ANNUAL REVIEWS

Design Principles for Noncentrosymmetric Materials

Xudong Huai and Thao T. Tran

Department of Chemistry, Clemson University, Clemson, South Carolina, USA;
email: xhuai@clemson.edu, thao@clemson.edu

ANNUAL REVIEWS CONNECT

www.annualreviews.org

- Download figures
- Navigate cited references
- Keyword search
- Explore related articles
- Share via email or social media

Keywords

noncentrosymmetric materials, nonlinear optical responses, magnetism,
skyrmions, topological protection, electronic structure
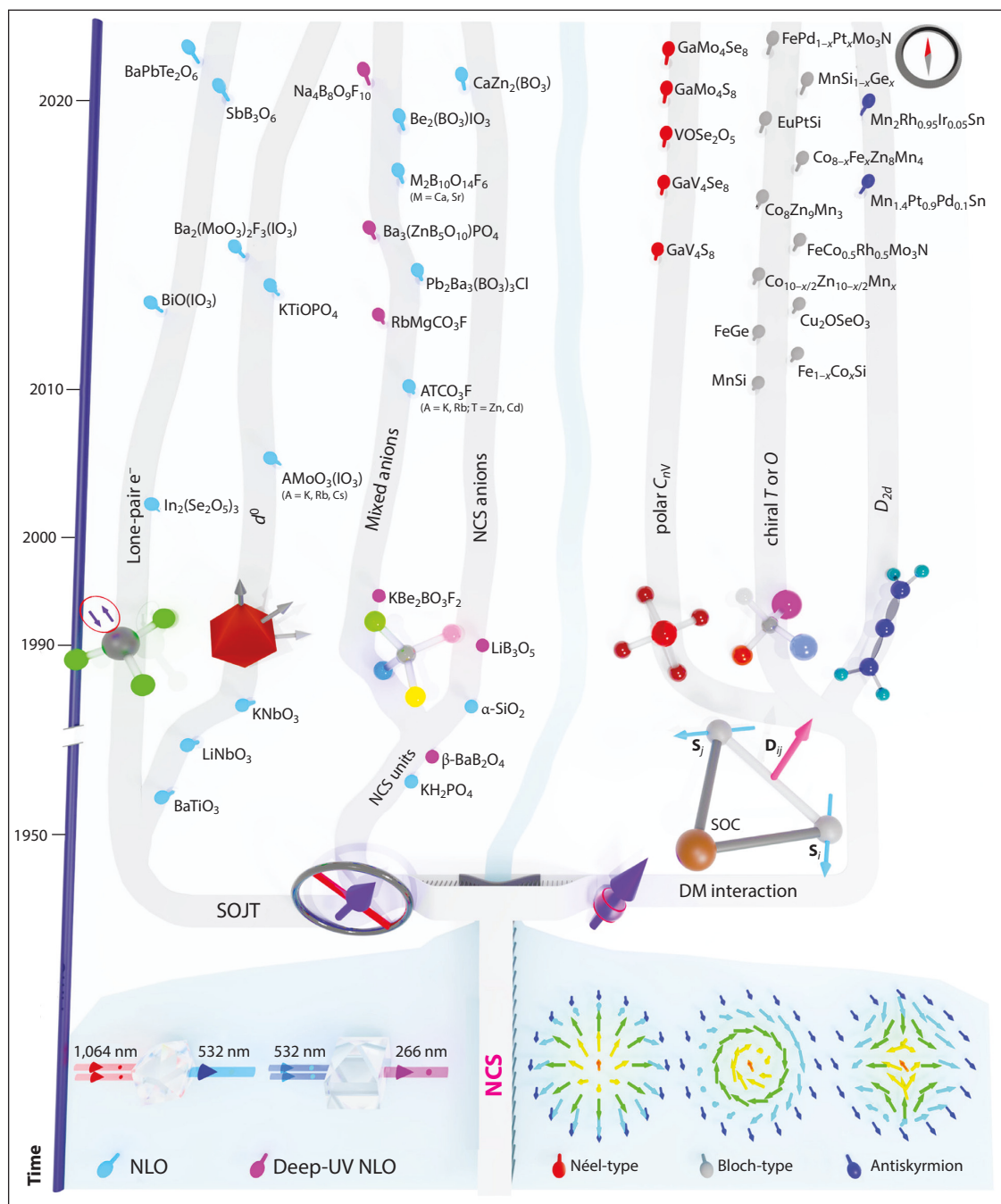
Abstract

Noncentrosymmetric (NCS) materials feature an exciting array of func-
tionalities such as nonlinear optical (NLO) responses and topological spin
textures (skyrmions). While NLO materials and magnetic skyrmions display
two different sets of physical properties, their design strategies are deeply
connected in terms of atomic-scale precision, structural customization, and
electronic tunability. Despite impressive progress in studying these systems
separately, a joint road map for navigating the chemical principles for NCS
materials remains elusive. This review unites two subtopics of NCS systems,
NLO materials and magnetic skyrmions, offering a multifaceted narrative
of how to translate the often-abstract fundamentals to the targeted func-
tionalities while inviting innovative approaches from the community. We
outline the design principles central to the desired properties by exemplify-
ing relevant examples in the field. We supplement materials chemistry with
pertinent electronic structures to demonstrate the power of the fundamen-
tals to create systems integration relevant to foreseeable societal impacts in
frequency-doubling instrumentation and spin-based electronics.

1. INTRODUCTION

Noncentrosymmetric (NCS) materials, lacking spatial inversion symmetry in their structure, are at the forefront of recent technological advances in optical frequency doubling and spintronics (1–12). Nonlinear optical (NLO) crystals harness fundamental light–matter interactions to generate an efficient exchange of energy from one frequency to another through the second-harmonic generation (SHG) process (13–22). This unique property enables numerous photonic applications of solid-state lasers in photolithography, photoemission spectroscopy, and medical and quantum information technology (13–22). Although NLO materials have uses in a wide spectral window ranging from infrared and near-infrared to visible, ultraviolet (UV), and deep-UV regions (19), this review focuses on visible to deep-UV systems. The versatility of NLO complexes possessing SHG at 1,064 nm offers powerful approaches for laser-based systems integration (3, 4, 19). On the other hand, deep-UV NLO-active materials capable of producing coherent radiation, especially those that can output 266 nm and 177.3 nm radiation with increased photon energy and high spectral resolution, feature important functionalities including precise micromachining, sensitive detection, and attosecond pulse generation (1, 14, 23–25). Two fundamental criteria required for creating NLO materials are the chemistry of main-group elements or d^0/d^{10} cations and the lack of inversion symmetry in the structure (3, 4, 19).

NLO crystals provide tremendous promise directly relevant to the current needs of advanced energy and information technologies; nevertheless, this is not the singular benefit of functional materials with broken spatial inversion symmetry. Integrating magnetism into NCS frameworks through unpaired electrons of transition metals opens up a viable pathway to realizing topologically distinct spin states (skyrmions), a prerequisite for spintronic architectures (7, 8). These nanoscale topological particles in real space exhibit exceptional electronic properties attributable to their capabilities to transmit, process, and store information with low-power operations (11, 12). The application of magnetic skyrmion materials has been envisaged in the fields of quantum information science and spintronics as scientists seek topological protection, a unique state wherein physical behaviors of spins are insensitive to perturbations such as lattice imperfections, environmental fluctuations, and room-temperature operations (10). Systems possessing appreciable Dzyaloshinskii–Moriya (DM) asymmetric exchange interactions facilitated by suitable coupled fundamental physical entities such as spins, orbitals, and phonons (7, 8) underlie the emergence of skyrmions in NCS magnets. Even though these topological phases have also been realized in centrosymmetric magnets and thin-film heterostructures with different underpinning mechanisms (26–35), this review capitalizes on the design considerations of bulk NCS magnetic skyrmion materials.

Despite tremendous achievements in investigating these two NCS classes separately, scientists still strive to unite atomic-scale precision with structural and electronic tunability to arrive at innovative and novel functional systems pertaining to ongoing material challenges for both science and instrumentation. While the two families of NLO materials and magnetic skyrmion hosts may appear to be entirely isolated islands, their chemical design principles are in fact fundamentally connected in terms of atomic-scale precision, structural customization, electronic adjustment, frontier orbital filling, and ligand effects. Thus, having a combined overview of the design considerations rooted in chemical logic for these two NCS material classes offers a multidimensional elucidation of how to effectively translate the often-abstract fundamentals to tangible and useful functionalities of interest (**Figure 1**). Furthermore, as light has been envisioned as a means to modulate the spin state of quantum systems that are anticipated to solve complex problems in computing, communicating, and sensing (36), this review intends to invite creative ideas and new approaches from the materials community for harmoniously synchronizing spin and photon degrees of freedom for previously untapped adventures in materials design and development.

(*Caption appears on following page*)

Figure 1 (*Figure appears on preceding page*)

A road map for navigating the design principles of NCS materials for NLO properties and magnetic skyrmion systems. Two main pathways leading to NLO materials involve NCS anion units and/or central cations susceptible to SOJT distortions. For magnetic skyrmion materials, the underlying mechanism is the DM asymmetric exchange interaction enhanced by integrating spins into NCS lattices and by large SOC. The emergence of Néel-type skyrmions, Bloch-type skyrmions, and antiskyrmions is driven by the underlying lattice symmetry of polar C_{nv}, chiral T or O, and the D_{2d} point group, respectively. While examples of these NCS materials, especially NLO crystals, are abundant, only a few of them are listed to exemplify the design principles and at the same time ensure clarity for the reader. Abbreviations: DM, Dzyaloshinskii–Moriya; NCS, noncentrosymmetric; NLO, nonlinear optical; SOC, spin–orbit coupling; SOJT, second-order Jahn–Teller; UV, ultraviolet.

In this review, we describe how the atomic-level design innate to the chemistry of NCS materials enables an exciting array of physical properties ranging from NLO and deep-UV NLO crystals to skyrmion systems (**Figure 1**). We start with guiding principles associated with each class and then use examples to demonstrate how a particular chemical path leads to a specific property. We highlight some challenges and opportunities for developing and converging the two optical and magnetic pathways in NCS materials.

2. NONLINEAR OPTICAL MATERIALS

2.1. Guiding Principles

For functional frequency doubling to be realized in the solid state, a crucial step from a design consideration perspective is to identify the fundamental aspects necessary to generate NLO and/or deep-UV NLO responses. One has to take into account materials requirements for SHG phenomena and UV transparency. These key criteria can be translated into design parameters, including broken spatial inversion symmetry, wide band gap, large SHG coefficient, appropriate birefringence, and chemical stability.

2.1.1. Second-harmonic generation.
An electric field from a light source interacts with the solid to induce a bulk polarization, P, proportional to the strength of the electric field E (37),

$$P = \varepsilon_0 \chi_{ijk}^{(1)} E. \qquad 1.$$

In nonlinear spectroscopy, the interaction of high-intensity electric fields generates a polarization response, which is not linear but has contributions from higher-order terms (37),

$$P = \varepsilon_0 \chi_{ijk}^{(1)} E + \varepsilon_0 \chi_{ijk}^{(2)} EE + \varepsilon_0 \chi_{ijk}^{(3)} EEE + \dots, \qquad 2.$$

where $\chi_{ijk}^{(2)}$ and $\chi_{ijk}^{(3)}$ are the second- and third-order susceptibilities.

Here we particularly focus on the second-order response to the polarization. The second-order term $\chi_{ijk}^{(2)}$ is crucial since it results in finite values of the susceptibility for systems wherein spatial inversion symmetry is broken.

By taking into account the electric field $E = E_1 \cos\omega t$, the second-order polarization can be expressed as the equation

$$P^{(2)} = \varepsilon_0 \chi_{ijk}^{(2)} (E_1 \cos\omega t)^2 \; = \; {}^1\!/_2 \varepsilon_0 \chi_{ijk}^{(2)} E_1^{\,2} (1 + \cos 2\omega t)^2, \qquad 3.$$

where ω is the angular frequency of the light (37).

When the dipole oscillates at twice the frequency of the incident radiation, 2ω, this leads to a phenomenon known as SHG. Equation 3 underlies the wavelength-dependent behavior of SHG. The second-order susceptibility is often described as the SHG coefficient,

$$d_{ijk} = {}^1\!/_2 \chi_{ijk}^{(2)}, \qquad 4.$$

where d is a tensor (37).

The fundamental and second-harmonic waves travel at different speeds owing to the inverse of their corresponding reflective indices. To maximize SHG efficiency, criteria such as appropriate electronic structures and lattice symmetries are required to match the wave vectors and the phases of fundamental and second-harmonic lights (37). A powder technique to evaluate the SHG response of materials was proposed by Kurtz & Perry (38). Phase-matching occurs when the phase velocity of the fundamental wave equals that of the second-harmonic wave. The phase-matching behavior is observed when the SHG efficiency increases with the particle size and reaches a plateau (38, 39). By contrast, nonphase matching occurs when the SHG efficiency achieves a maximum and then decreases as particle size increases (38, 39).

Taken together, these fundamentals clearly demonstrate that materials that may feature NLO behavior must crystallize in one of the NCS crystal classes. The cubic 432 point group nevertheless presents an exception (40). Although this point group is NCS, all the components of the susceptibility tensor have equal and opposite magnitude, yielding an SHG-inactive response (40). To enable the tunability of the SHG efficiency and phase-matching behavior of NLO materials, one can adjust the lattice symmetry, frontier orbitals, electronic structure, and polarizabilities. It is also worth keeping in mind that the NLO property goes hand-in-hand with the incident wavelength; that is, the SHG output is fundamentally dependent on the radiation input (**Figure 1**).

2.1.2. Deep-ultraviolet nonlinear optical property.
To take a functional NLO material to the deep-UV region (**Figure 1**), a few more requirements need to be met in addition to the lack of spatial inversion symmetry as aforementioned.

- A wide-UV transparency window is an important ingredient for deep-UV NLO materials. NLO materials ought to exhibit an absorption edge $\lambda < 200$ nm or energy gap $E_g > 6.2$ eV (1, 2, 5). This implies that central metal cations having partially filled d or f states should not be incorporated. However, cations with filled d or half-filled f states can be considered, as their electronic structures hinder unfavorable electronic transitions. Main-group metals make excellent choices for deep-UV NLO materials owing to their valence s and p states often being at low energy, broadening the band gap.
- A large SHG coefficient, d_{ij}, plays an essential role to arrive at a deep-UV NLO property. Materials having large SHG coefficients are capable of doubling photon energy with high efficiencies. To achieve a functional NLO material in the deep-UV region, the SHG coefficient d_{ij} should be comparable to or greater than that of KH_2PO_4 (KDP, at 1,064 nm) and at least 25% of that of β-BaB_2O_4 (at 532 nm) (1, 2, 5, 39). Maker fringe measurements, which require sizable crystals, can be used to determine individual SHG coefficients d_{ij} values (41).
- Phase-matching in the UV and deep-UV region is a key parameter that is factored in the capability of displaying efficient frequency doubling phenomena. To effectively produce coherent light through the SHG, the harmonic and fundamental wave ought to have the same propagation speed, that is, the phase-matching behavior $n(2\omega) = n(\omega)$, where n is the refractive index (42). In the UV and deep-UV region, while small birefringence Δn does not meet the phase-matching condition, large birefringence $\Delta n > 0.10$ leads to unfavorable walk-off processes. Thus, a moderate birefringence, $0.07 \leq \Delta n \leq 0.10$, is suitable for achieving phase-matching (1, 2, 5, 42).
- Chemical stability and crystal quality are vital to the ability to incorporate an NLO material into operational constructs. Even when all the requirements discussed above are fulfilled, high-quality, large NLO crystals with large laser damage thresholds are needed for integrating them into functional instrumentation (1, 2, 5). This underlines the importance of chemical stability, crystal quality, and processing of NLO materials.

These fundamental guidelines described in Section 2.1 outline the criteria for designing NLO and deep-UV NLO materials (**Figure 1**) while preparing for the discussion in Section 2.2 on design strategies for translating the atomic-level chemistry of locally NCS anionic units and/or central metals susceptible to second-order Jahn–Teller (SOJT) distortion into rationally produced NLO materials (Section 2.2).

2.2. Design Strategies

Following the guiding principles for NLO and deep-UV NLO systems, the next step is to determine the chemical design pathways feasible to bring about these physical phenomena in real materials. The common chemical strategies for creating targeted NLO materials one can consider are NCS building units (asymmetric anions and mixed anions) and SOJT (d^0 cations and lone-pair electrons), which can be combined to produce SHG.

2.2.1. Noncentrosymmetric units.
Asymmetric anions inherent to broken inversion symmetry, such as borates, carbonates, nitrates, sulfates, and phosphates, can be used to induce locally asymmetric entities into forming the extended NCS structure (**Figure 1**). This approach has been demonstrated by extensive studies that successfully constructed worthwhile paths rooted in the chemical diversity of these NCS anions for generating new NLO materials (43–58). Chen et al. (59) proposed the anionic group theory based on the quantum-mechanical perturbation theory of the NLO effect. This concept centers on how the microscopic anion constituents of NCS materials, such as electronic polarization, spatial alignment, and density of states (DOS), impact macroscopic NLO responses (59). For example, β-BaB_2O_4 exhibits the coarrangement of BO_3^{3-} trigonal entities, mixing between B-p and O-p states near the Fermi level, and wide band gap (**Figure 2**), resulting in large SHG susceptibilities in the deep-UV region (60). It has also been suggested that the O-p states involved in NCS anion units and in the valence band maximum contribute significantly to NLO effects while the energies of these orbitals are responsible for the SHG magnitude (60).

Mixed-anion approaches involve the combination of mixed anions to break spatial inversion symmetry in the resulting structure, thus giving rise to SHG properties (**Figure 1**) (24, 61–79). In addition, appropriate choices and custom alignment of anionic units can yield large NLO responses while widening the transparency window to the deep-UV region (**Figure 1**) (24, 61–79).
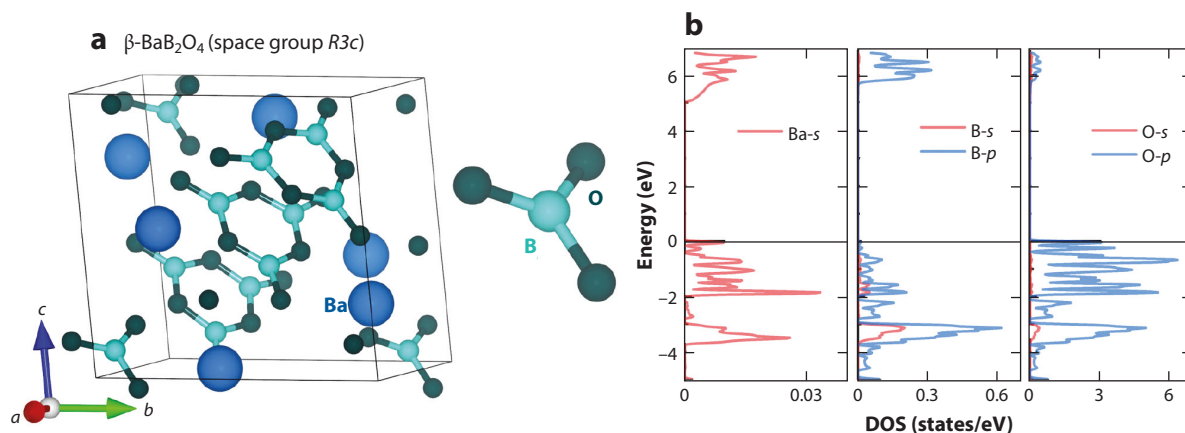

a β-BaB_2O_4 (space group *R3c*)

b

Figure 2
β-BaB_2O_4 (*a*) crystal structure featuring the coalignment of the BO_3^{3-} asymmetric anions and (*b*) density of states (DOS) showing orbital overlap between B-p and O-p states near the Fermi level.
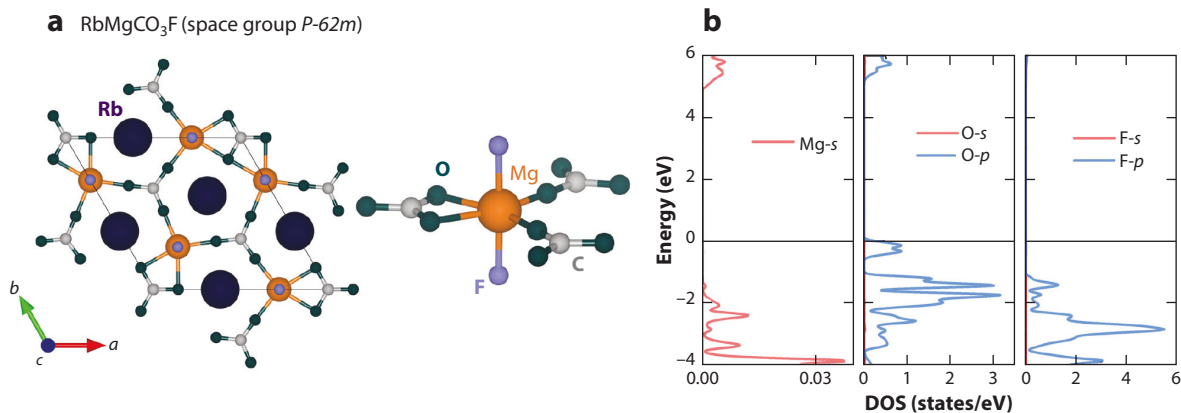
a RbMgCO₃F (space group *P-62m*)

b

Figure 3

RbMgCO₃F (*a*) crystal structure featuring mixed CO_3^{2-} and F^- anions bonded to Mg^{2+} and (*b*) density of states (DOS) showing the significant contribution of the O-*p* states of the CO_3^{2-} groups at both the valence band maximum and the conduction band minimum.

RbMgCO₃F is a deep-UV NLO material exhibiting large SHG responses, four times that of KDP at 1,064 nm and 0.6 times that of β-BaB₂O₄ at 532 nm. The chemistry of this material poses a suitable example for demonstrating the feasibility of this heteroanionic design strategy. Mixed CO_3^{2-} and F^- anions with fundamentally different bonding characters are combined to effectively improve acentric displacements in RbMgCO₃F (61). The CO_3^{2-} asymmetric anions with conjugated π-bonding coalign in the *ab* plane, whereas the F^- isotropic compact anion takes the axial position along the *c* direction (**Figure 3**) (61). The top of the valence band and the bottom of the conduction band of RbMgCO₃F are mainly composed of the O-*p* states of the CO_3^{2-} groups, which contribute primarily to the wide energy gap and considerable optical anisotropy of this material in the deep-UV spectrum (**Figure 3**) (61). Relevant examples and insights of heteroanionic engineering in other functional and quantum materials to construct targeted properties by modifying anions of dissimilar size, charge, and electronegativity have been experimentally and computationally illustrated (80–82). These strategies can be adopted for use in accelerating the discovery and development of NLO materials.

Proper assembly of locally asymmetric anionic entities or mixed anions resulting in an extended NCS framework offers a viable strategy for producing NLO materials. Furthermore, metal ions prone to SOJT perturbation make excellent choices for initializing the microscopic cation environment with acentric displacements.

2.2.2. Second-order Jahn–Teller distortion. The SOJT effect is associated with changes in structures attributable to a nondegenerate ground state mixing with a low-lying excited state; the first-order Jahn–Teller distortion, on the other hand, gives rise to molecular distortions owing to degenerate electronic ground states. The SOJT distortion occurs when the energy gap between the highest occupied molecular orbital (HOMO) and the lowest unoccupied molecular orbital (LUMO) is narrow and the mixing of the HOMO and LUMO is symmetry-allowed.

Octahedrally coordinated d^0 transition metal ions, such as Ti^{4+}, Nb^{5+}, and Mo^{6+}, are susceptible to the SOJT distortion and are often found in distorted coordination environments wherein the central cation is off-center from the octahedron of ligands. For these d^0 cations, overlapping between the HOMO and LUMO is symmetry-allowed, and the degree of mixing of the HOMO and LUMO tends to increase with the ratio of charge to radius of the d^0 cations (83). Using BaTiO₃ as an example, the SOJT distorted Ti^{4+} cation plays a vital role in the NLO response
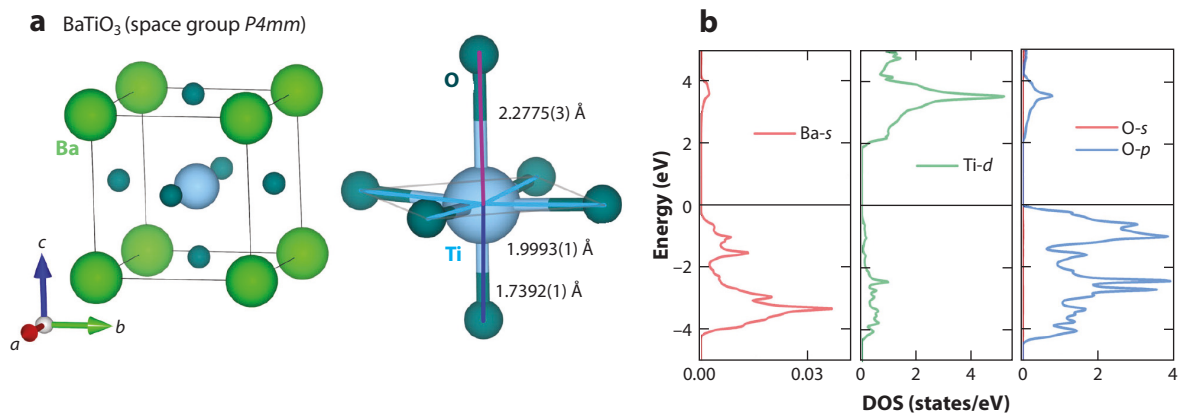
a BaTiO$_3$ (space group *P4mm*)

b

2.2775(3) Å

1.9993(1) Å

1.7392(1) Å

Figure 4

BaTiO$_3$ (*a*) crystal structure featuring the second-order Jahn–Teller distorted Ti^{4+} (d^0) cation environment and (*b*) density of states (DOS) showing the contribution of the Ti-*d* and O-*p* states of the distorted TiO$_6$ octahedra at both the valence band maximum and the conduction band minimum.

of this material ($\sim$10 times that of KDP at 1,064 nm) (39). The DOS of BaTiO$_3$ indicates that the Ti-*d* and O-*p* states of the distorted TiO$_6$ octahedra interact and make up the valence band maximum and the conduction band minimum, responsible for frequency doubling under optical excitation (**Figure 4**). Goodenough & Longo (84) demonstrated that a d^0 cation can distort in three manners: along the C_4, the C_2, or the C_3 axis. Additional insight into these distortions was elucidated by Kunz & Brown (83), namely that the structural deformation is driven not only by the d^0 electronic structure but also by other factors including bonding network, lattice incommensuration, and cation–cation repulsion. This cooperative distortion enables a tunable parameter at the cationic level while highlighting the dynamics between the chemistry of SOJT and NCS anion building units in constructing NLO materials (**Figure 1**) (85–92).

In addition to the d^0 cations, metal ions having lone-pair electrons (s^2), such as Sn^{2+}, Sb^{3+}, Bi^{3+}, Se^{4+}, Te^{4+}, and I^{5+}, experience electronic instability, yielding the distorted coordination environments (92–94). This can also be explained by the SOJT perturbation. A strongly antibonding HOMO, which is comprised of the s^2 lone-pair electrons, overlaps with the *p*-derived LUMO (*s*–*p* mixing), thus stabilizing the system and revealing stereoactive lone-pair electrons. This type of SOJT distortion offers an alternative strategy for using the locally asymmetric coordination environment of cations to construct globally NCS structures.

For example, the stereoactive lone-pair electrons of Bi^{3+} and IO$_3^-$ have been thought to contribute to the strong SHG of BiO(IO$_3$) ($\sim$12.5 times that of KDP at 1,064 nm) (95). The valence band maximum and conduction band minimum of BiO(IO$_3$) are mainly dominated by the lone-pair electrons of Bi (Bi-*s* and Bi-*p* states), those of the IO$_3$ group (I-*s* and I-*p* states), and the ligand O-*p* states, which facilitate significantly large NLO responses (**Figure 5**) (95). The inclusion of cations with lone-pair electrons has yielded fruition in the creation of NLO materials exhibiting appreciable SHG susceptibilities (**Figure 1**) (95–103).

It is worth noting that the participation of *d*-states or *sp*-states of a d^0 cation or a cation with stereoactive lone-pair electrons, respectively, typically occurs at high energy up in the valence band maximum and conduction band minimum, narrowing the band gap. Thus, while central cations with SOJT distortion make excellent choices for improving NLO responses at 1,064 nm, their electronic contribution to band structure tends to preclude them from being SHG-active in the deep-UV region (e.g., at 532 nm).
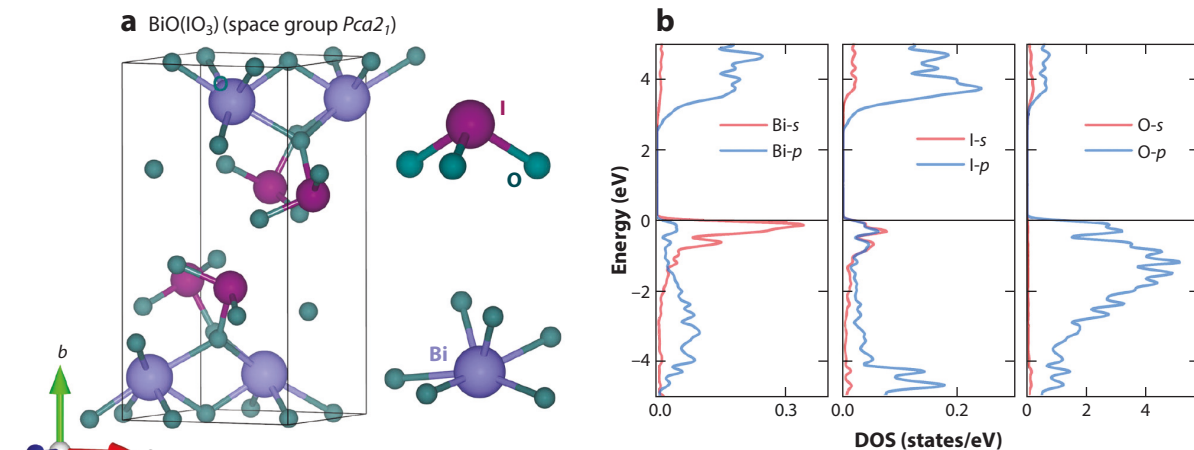
Figure 5

BiO(IO$_3$) (*a*) crystal structure featuring the second-order Jahn–Teller distorted IO$_3$ and Bi^{3+} environments with stereoactive lone-pair electrons and (*b*) density of states (DOS) showing the significant contributions of the lone-pair electrons of Bi (Bi-*s* and Bi-*p* states), those of the IO$_3$ group (I-*s* and I-*p* states), and the ligand O-*p* states at both the valence band maximum and the conduction band minimum.

Breaking spatial inversion symmetry in nonmagnetic NCS systems, guided by these aforementioned strategies, has led to the impressive progress in producing and developing NLO materials that are capable of generating coherent light with double the energy of the incident radiation in the targeted spectral region (**Figure 1**). This, however, naturally prompts the following questions: What if spin degrees of freedom are incorporated into NCS extended frameworks, and does this blaze an entirely new trail to achieving other novel functionalities while elevating NCS magnetic materials to the cutting edge of spin-based electronics? To answer, we turn to NCS magnetic skyrmion materials, which feature topologically nontrivial spin states.

3. NONCENTROSYMMETRIC SKYRMION HOST MATERIALS

3.1. Guiding Principles

The concept of skyrmions was first introduced in a nonlinear field theory by Skyrme (104, 105) to exemplify topological protection; that is, the topological integer number of these particles is unchanged even in the presence of continuous perturbations. The topologically protected property of skyrmions renders them appealing choices for robust information carriers in spin-based electronic architectures such as spintronics and quantum logic constructs (7, 8, 11, 106). The fundamental principle underpinning much of this phenomenon in NCS magnetic skyrmion materials is the enhancement of DM asymmetric exchange (**Figure 6**) in the presence of Heisenberg isotropic interaction (107, 108),

$$H_{DM} = \Sigma_{<ij>}\mathbf{D}_{ij} \cdot (\mathbf{S}_i \times \mathbf{S}_j), \qquad 5.$$

where H_{DM} is the spin Hamiltonian for DM exchange, $\mathbf{D}_{ij}$ is the DM vector, and $\mathbf{S}_i$ and $\mathbf{S}_j$ are spins at neighboring sites i and j.

The DM anisotropic interaction is facilitated by strong coupling of spin, orbital, and lattice components in the absence of spatial inversion symmetry in NCS magnets (7). These quantum effects are strongly correlated with the relativistic spin–orbit coupling (SOC), which tends to
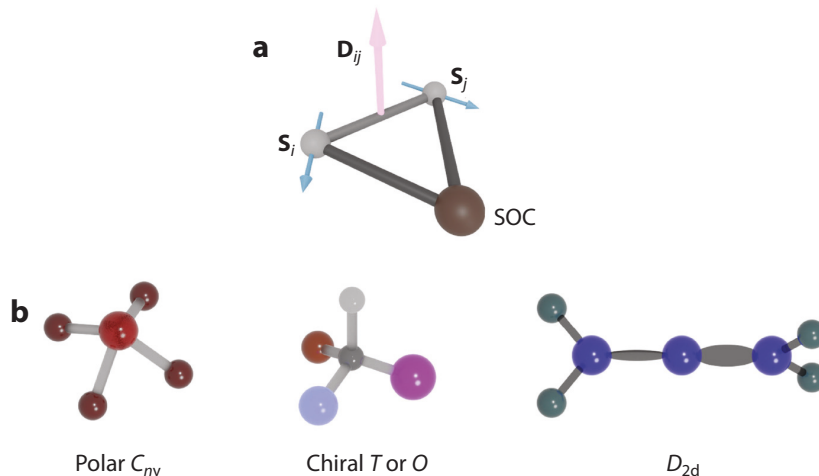
Figure 6

(*a*) Dzyaloshinskii–Moriya (DM) asymmetric exchange $\mathbf{D}_{ij}$ between $\mathbf{S}_i$ and $\mathbf{S}_j$ spins at neighboring sites i and j bolstered by broken inversion symmetry and large spin–orbit coupling (SOC). (*b*) Polar C_{nv}, chiral T or O, and D_{2d} lattice symmetry enhancing the DM interaction in noncentrosymmetric magnets.

rotate the mutual spin alignment (**Figure 6**). This gives rise to a cycloidal or helical structure at zero field while potentially forming skyrmion phases in a certain range of applied magnetic fields (7). It is worth noting that skyrmions emerge at finite field, and the evolution of these states of matter is a field-driven phase transition at a certain temperature, typically in the vicinity of the magnetic ordering temperature T_C or T_N (7). Critical magnetic field and temperature represent an estimate of the strength of the driving force necessary for these vortex-like winding spins. The experimental values of H_C and T_C in magnetic skyrmions are rather diverse and cannot be explained by the simple model rooted in DM exchange alone (7). An intricate ensemble of DM asymmetric interaction, Heisenberg symmetric exchange, SOC, and electron−phonon coupling effects ought to be considered to determine the origin of these phenomena. This deep understanding will enable the development of bottom-up assembly of spin-based architectures with precision, tunability, and scalability.

The size of skyrmions, typically ranging from 1 to 100 nm, can be estimated from the associated magnetic modulation wavelength, which is the ratio between the strength of the DM exchange and the Heisenberg interaction (7). Three typical types of these topological spin textures are Néel-type, Bloch-type, and antiskyrmions. Néel-type skyrmions feature a radical spin arrangement, whereas Bloch-type skyrmions exhibit a swirling spin configuration (**Figure 1**) (7). The evolution of antiskyrmions is characterized by alternating Néel- and Bloch-type moment rotations (**Figure 1**) (7).

These forms of topological spin phases are fundamentally driven by the crystallographic point group symmetry that can be mathematically illustrated by Lifshitz invariants, a form of the free energy to which the DM asymmetric exchange contributes (109),

$$L_{ij}^{(k)} = m_i \partial_k m_j - m_j \partial_k m_i, \qquad\qquad 6.$$

where i, j, and k are an arbitrary choice of x, y, and z Cartesian coordinates.

This term enhances spin twisting in the ij plane and propagation along the k direction while elucidating the core principle of how the underlying lattice symmetry influences the DM exchange energy density and thus the vorticity of magnetic skyrmions.

Even though skyrmions cast new light on topics of deep interest in the physics and materials chemistry communities, only a limited number of NCS magnets hosting these topological phases have been realized. As new skyrmion materials are discovered and developed, a more complete set of design principles will be established. Nevertheless, the current repertoire of NCS skyrmion materials can be classified into three main design strategies on the basis of the underlying lattice symmetry: polar C_{nv}, chiral T or O, and D_{2d} point groups hosting Néel-type skyrmions, Bloch-type skyrmions, and antiskyrmions, respectively (**Figure 6**).

3.2. Design Strategies

Following the aforementioned guiding principles underpinning the emergence of skyrmions, the chemical design strategies across various skyrmion materials are the polar C_{nv}, chiral T or O, and D_{2d} point groups of the lattice symmetry.

3.2.1. Polar C_{nv}.
GaM_4Q_8 (M = V or Mo, Q = S or Se) magnetic semiconductors, a family of lacunar spinels wherein tetrahedral M_4 clusters play a vital role in the polar achiral C_{3v} symmetry of these materials, have been demonstrated to host Néel-type skyrmions (**Figure 1**) (110–117). Taking $GaMo_4Se_8$ as an example, it has been illustrated that the room temperature cubic structure is susceptible to two competing Jahn–Teller distortions, resulting in the ground state $R3m$ and a metastable phase (114). The $R3m$ phase of $GaMo_4Se_8$, which is analogous to that of $GaMo_4S_8$, features two sets of Mo–Mo bonds in the tetrahedral Mo_4 cluster with each Mo coordinated with six Se(S) atoms (**Figure 7**). Spin-polarized density-functional theory calculations showed that the valence band maximum of $GaMo_4S_8$ is mainly dominated by competing overlaps of the Mo-d–Mo-d and Mo-d–S-p states (**Figure 7**) (118). This overlapping is tied to the observed magnetic property; that is, the tetrahedral Mo_4 clusters have both intracluster and intercluster interactions, bolstering anisotropic exchange (118). These features of the crystal and electronic structure of GaM_4Q_8 work in favor of increasing DM asymmetric interaction in the polar C_{3v} lattice and thus the emergence of a cycloidal magnetic ground state and Néel-type skyrmion under an applied field (110–118).

In addition to C_{3v} symmetry, the C_{4v} point group offers an alternative route to stabilizing Néel-type skyrmions as exemplified in $VOSe_2O_5$ (**Figure 1**) (119, 120). The polar crystal structure of
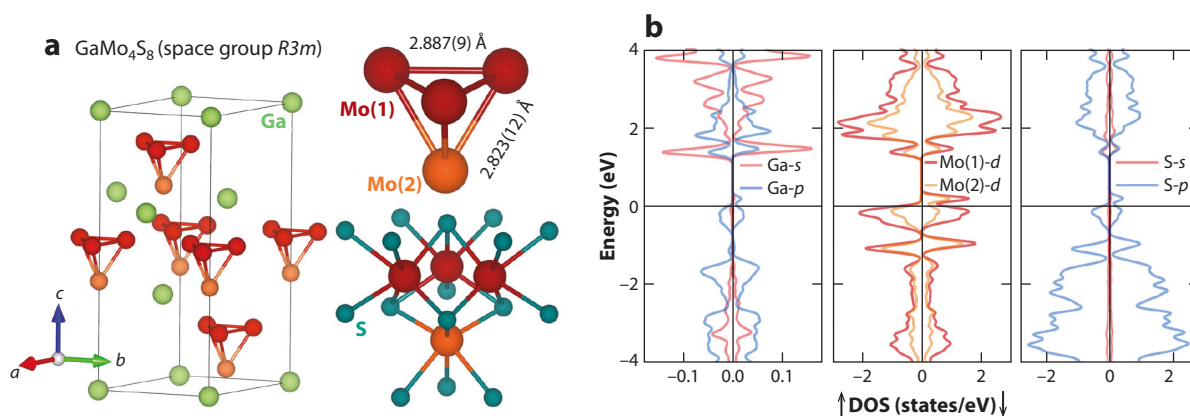

Figure 7

$GaMo_4S_8$ (*a*) crystal structure (S atoms have been left out for clarity) featuring Mo_4 tetrahedral clusters having two distinct Mo(1) and Mo(2) sites with two sets of Mo–Mo bonds and each Mo coordinated with six S atoms and (*b*) density of states (DOS) showing competing overlaps of the Mo-d–Mo-d and Mo-d–S-p states.
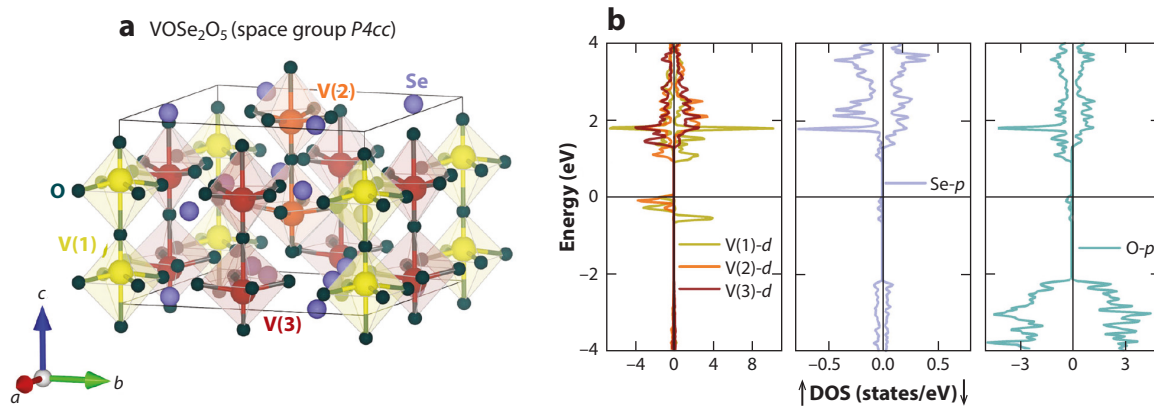
a VOSe$_2$O$_5$ (space group *P4cc*)

b

Figure 8

VOSe$_2$O$_5$ (*a*) crystal structure featuring three distinct chains of distorted VO$_6$ octahedra along the *c*-axis and asymmetric SeO$_3$ groups owing to the lone-pair effect and (*b*) density of states (DOS) showing significant overlap of the polarized V-3*d*, O-2*sp*, and Se-4*sp* states around the Fermi level.

this material consists of three distinct chains of the corner-shared VO$_6$ octahedra running along the *c*-axis direction that are linked by the SeO$_3$ trigonal pyramids (121). The locally distorted SeO$_3$ coordination environment is governed by the nonbonded electron pair SOJT effect, and the stereoactive lone-pair electrons of the SeO$_3$ units reside in the Se-4*sp* states. Spin-polarized density-functional theory calculations with electron–electron repulsion energy *U* resulted in substantial overlaps between the V-3*d*, O-2*sp*, and Se-4*sp* states around the Fermi level, giving rise to appreciable intrachain and interchain magnetic interactions between the V^{4+} spins (**Figure 8**) (121). VOSe$_2$O$_5$ exhibits a cycloidal magnetic state at zero field and an incommensurate spin texture at lower temperatures. Under a magnetic field, a Néel-type skyrmion is observed along the polar *c*-axis (119). The results indicate that incorporating stereoactive lone-pair electrons in the valence band maximum in the presence of partially filled *d*-states of transition metals enhances DM anisotropic interaction in the polar C_{4v} lattice symmetry, thereby forming Néel-type topological spin phases (119–121).

Inspired by these insights, recent studies in polar NCS magnets of transition metal iodates have illustrated the viability of linking stereoactive lone-pair electrons (I-*s*/*p* states) to increased anisotropy of magnetic interactions (122, 123). In Fe(IO$_3$)$_3$, the polarized Fe-*d* states, responsible for magnetism, overlap with the O-*p* and I-*s*/*p* states, contributing to the valence band maximum (**Figure 9**). The DM asymmetric exchange of Fe(IO$_3$)$_3$ was estimated from neutron diffraction experiments to be approximately 18% of the strength of the Heisenberg interaction along the polar *c*-axis (122). The associated magnetic modulation period of the DM-driven incommensurate order is 18 nm, suggesting that putative finite-field topological spin textures would have compact size, comparable to the helix wavelength (122). The evidence of appreciable DM exchange and the zero-field spiral antiferromagnetic magnetic ground state promises to enlarge the bottom-up development of new skyrmion materials.

3.2.2. Chiral *T* or *O*. NCS magnets having chiral *T* or *O* point group symmetry, such as B20 structures (MnSi, FeGe, Fe–Co–Si), β-Mn types (Co–Zn–Mn, FePd$_{1-x}$Pt$_x$Mo$_3$N), and Cu$_2$OSeO$_3$, are attractive materials for stabilizing Bloch-type skyrmions (**Figure 1**) (124–136). The universal feature in these crystal lattices is chirality in which a left-handed and a right-handed structure are not superimposed. This manifestation affords opposite spiral arrangement of atoms in the structure, thus breaking spatial inversion symmetry.
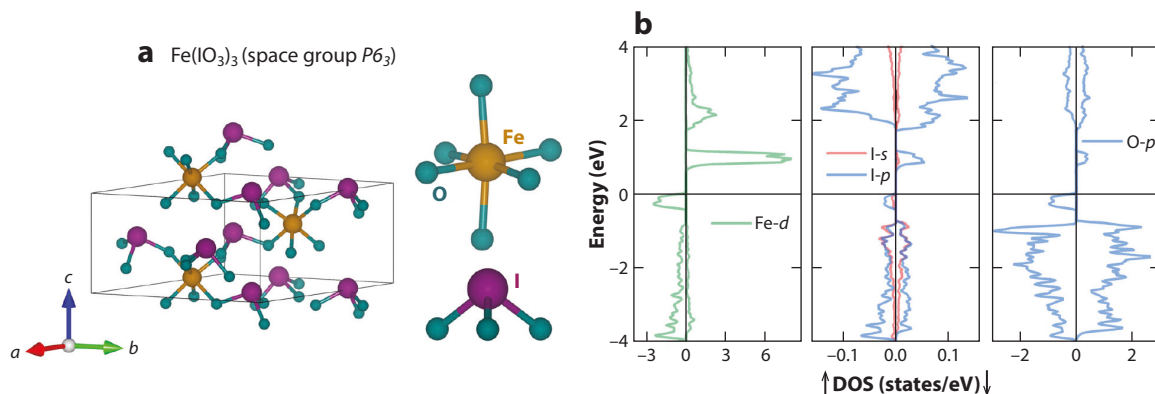
a Fe(IO$_3$)$_3$ (space group $P6_3$)

b

Figure 9

Fe(IO$_3$)$_3$ (*a*) crystal structure featuring a macroscopic electric polarization along the *c*-axis direction, building units of FeO$_6$ octahedra, and an IO$_3$ trigonal pyramid with stereoactive lone-pair electrons and (*b*) density of states (DOS) showing overlap of the polarized Fe-*d*, O-*p*, and I-*s/p* states.

The crystal and electronic structure of MnSi, a seminal Bloch-type skyrmion host, can help illustrate this concept (**Figure 10**) (137). Mn and Si atoms possess chiral stacking along the body-diagonal [111] direction, which has been considered the critical factor for the enhanced DM exchange (7, 137). This is supported by the spin-polarized DOS of MnSi, in which substantial overlapping between the Mn-*d* and Si-*p* states is evident (**Figure 10**). The Mn-*d* derived states are polarized, direct proof of Mn contributing to magnetism. The spin of Mn polarizes the Si-*s* and Si-*p* electrons, enhancing the coupling of spin, orbital, and lattice degrees of freedom. This inter-action twists the direction of every neighboring spin moment in MnSi, generating the evolution of a helical magnetic ground state at zero field and a swirling Bloch-type skyrmion phase under finite field (7).

Cu$_2$OSeO$_3$, the first example of an NCS magnetic insulator hosting skyrmions, adopts the same space group with B20-structure MnSi ($P2_13$) (**Figure 1**); however, the arrangements of the atoms in the structure are more complex (129). The magnetic Cu^{2+} cations take up two distinct
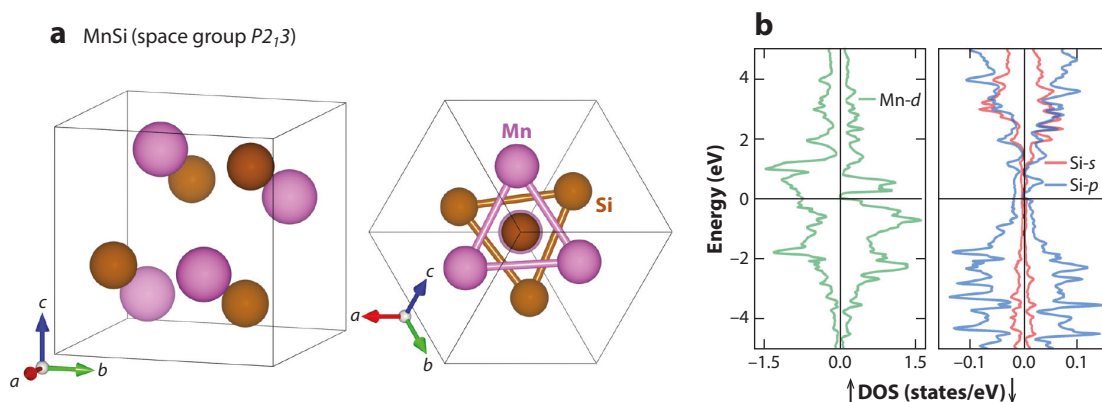

a MnSi (space group $P2_13$)

b

Figure 10

MnSi (*a*) crystal structure featuring opposite spiral stacking of Mn and Si atoms and (*b*) density of states (DOS) showing overlap between the polarized Mn-*d* and Si-*s/p* states.
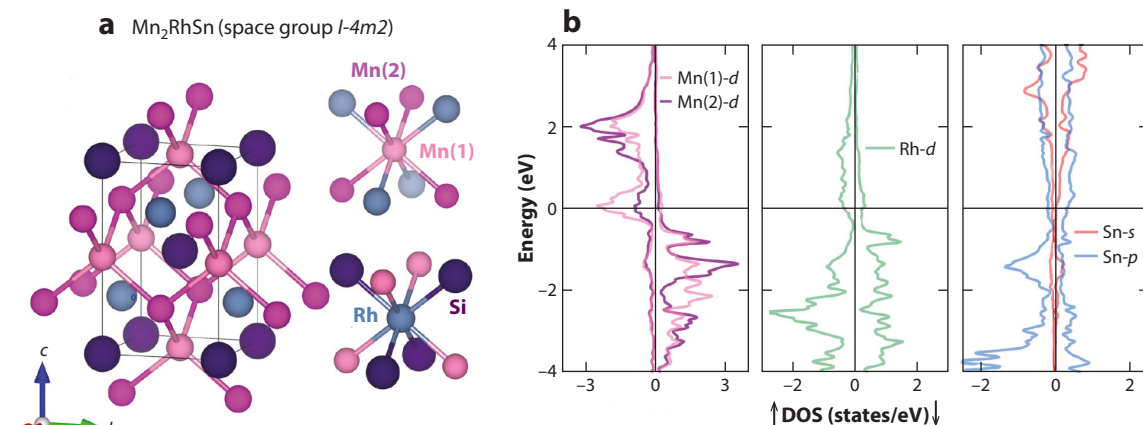
a Mn$_2$RhSn (space group *I-4m2*)

Figure 11

Mn$_2$RhSn (*a*) crystal structure featuring the D_{2d} symmetry of Mn(1) and Mn(2) crystallographically distinct sites and (*b*) density of states (DOS) showing competing overlap between the Mn(1)-*d*–Mn(2)-*d* and Mn(1)-*d*–Rh-*d*/Mn(2)-*d*–Sn-*p* states.

sites with different symmetries, that is, Cu(1) in a square pyramidal coordination and Cu(2) in a trigonal bipyramidal environment. The acentric structure of Cu$_2$OSeO$_3$ is in part attributable to the contribution of the distorted SeO$_3$ unit with the lone-pair electron effect. This leads to complex competing magnetic exchange interactions in this material. Cu(1)–Cu(1) spins interact in a ferromagnetic fashion while Cu(1)–Cu(2) sites communicate antiferromagnetically (129). Nevertheless, the magnetic phase diagram of Cu$_2$OSeO$_3$ bears considerable resemblance to those of B20 metallic magnets (129). At zero field, the magnetic ground state of Cu$_2$OSeO$_3$ displays a helical structure with a long modulation period of 63 nm. Under a finite field along the [111] direction, a Bloch-type skyrmion state emerges right after $T_C = 60$ K. These magnetic states of the NCS chiral Cu$_2$OSeO$_3$ material are governed by an increased DM asymmetric exchange interaction (129).

3.2.3. D_{2d}. Recent studies have expanded the family of NCS magnetic skyrmions by elegantly showcasing antiskyrmions in Mn$_{1.4}$Pt$_{0.9}$Pd$_{0.1}$Sn and Mn$_2$Rh$_{0.95}$Ir$_{0.05}$Sn with D_{2d} point group symmetry (analogous to the Mn$_2$RhSn structure) (**Figure 1**) (138–141). This opens a worthwhile avenue for exploiting the tunability of Heusler materials to stabilize the topological spin texture that features varying Bloch- and Néel-type moment directions (138–140). The size of the antiskyrmion is quite large, ~150 nm, comparable to the modulation period of the helix structure (139). In the Mn$_2$RhSn parent structure, Mn atoms occupy two crystallographic sites, Mn(1) and Mn(2), featuring D_{2d} symmetry (**Figure 11**) (142). At the Fermi level, there is competing interaction between the Mn(1)-*d*–Mn(2)-*d* and Mn(1)-*d*–Rh-*d*/Mn(2)-*d*–Sn-*p* states (**Figure 11**). This electronic structure aids in the increase of asymmetric DM exchange interaction in the D_{2d} underlying lattice, resulting in the unique vorticity of the antiskyrmion structure in Mn$_{1.4}$Pt$_{0.9}$Pd$_{0.1}$Sn and Mn$_2$Rh$_{0.95}$Ir$_{0.05}$Sn (138–140).

4. CHALLENGES AND OPPORTUNITIES

Based on the design principles for NCS compounds discussed in Sections 2 and 3, can new NLO and skyrmion materials be rationally created using judicious strategies? The answer is probably yes. While the fundamentals enable useful guidance on how the underlying chemistry of NCS materials synchronizes with the rigorous criteria that must be fulfilled to generate the targeted

physical properties, experiments sometimes have a different idea. Even though NLO and magnetic skyrmion materials exhibit different functionalities, these systems experience similar challenges in synthesis and materials growth. This is in part attributable to the intrinsic constraints of simultaneously modulating both local and extended arrangements of atoms to break global spatial inversion symmetry in the resulting structure. However, appropriately choosing synthetic techniques on the basis of their predisposition toward chemically controlled synthesis and crystal growth can improve the odds of attaining desired NCS phases (143–150). When design considerations and proper experimental choices are taken into account, arriving at NCS materials of interest is still inevitably uncertain. So then, why bother? There are at least two enormous advantages to contemplate when we are willing to let go of the pursuit of the absolute. First, constructing a worthwhile pathway deeply rooted in materials chemistry to design and create new and useful systems with desired functionalities will challenge the conventional trial-and-error wisdom, accelerating the innovation of unprecedented materials pertinent to the current needs of advanced energy and information technology research. Second, the research journey of applying and pondering design strategies for NCS multifunctional and quantum materials will potentially unfold other exciting and groundbreaking realizations outside of the original sphere that would not be possible otherwise.

5. FUTURE PROSPECTS FOR NONCENTROSYMMETRIC MATERIALS RESEARCH

The design principles for NCS materials, articulated in this brief review, provide a playground to further explore new NLO crystals featuring large SHG responses in the spectral window of interest and previously undiscovered magnetic skyrmion hosts with tunable conditions (temperature, magnetic and electric fields) at which topological spin phases emerge. Although the focus of this review is on the chemistry of NLO and skyrmion materials, the broad reach of research in the field is astonishing, spanning from solid-state chemistry to materials science, engineering, and condensed matter physics. In these areas, materials growth, theoretical computations, and deep characterizations of structural, optical, electronic, and magnetic properties are rapidly progressing. Yet there is value in taking a small step back to reflect on the fundamentals underpinning many of these functionalities. In particular, the vital roles of chemical logic, orbital overlapping, electronic structure, and underlying lattice symmetry have been emphasized.

In addition, modifying chemical customization and tuning electronic structure from NLO crystals to skyrmion hosts and vice versa offer tremendous promise for achieving new classes of multifunctional and quantum materials. Replacing transition metals in NCS magnetic skyrmions with main-group elements can lead to an exciting frontier for developing new NLO materials with tunable SHG efficiencies and spectral windows. On the other hand, the remarkable library of reported NLO compounds can be translated into a jumping-off point for exploring previously untapped NCS magnetic skyrmion materials. This crossing can be done by computationally selecting NLO systems with the underlying lattice symmetry of polar C_{nv}, chiral T or O, or D_{2d}, a prerequisite for skyrmion formation, and then sensibly substituting central s/p cations with d/f elements with partially filled valence shells to induce magnetism in these NCS frameworks. A dialogue among scientists that have expertise in different areas such as machine learning, materials chemistry, and condensed matter physics but share similar interests may prompt fruitful partnerships in catalyzing a platform for uncovering many more exciting breakthroughs and advancing new knowledge in the field. This review would be incomplete if we did not mention recent studies of materials requirements for combining optics and electronics to improve the control of quantum bits and the electromagnetic environment necessary for high-fidelity

quantum operations (36). This quest poses another highly appealing prospect for bridging the two seemingly parallel pathways of NCS optical and spin-based systems that will bring about completely renewed and unmatched capabilities of integrated systems for addressing the grand materials challenges directly relevant to future technological and societal impacts.

We hope that this brief review demonstrates the incredible progress made by scientists in the field and at the same time sparks more cross-disciplinary investigations in contemporary materials research. Through fundamental design principles and concerted, collaborative studies, the insights and knowledge necessary for innovative materials to transform the forefront of science and instrumentation are within our reach.

DISCLOSURE STATEMENT

ACKNOWLEDGMENTS

LITERATURE CITED

1. Halasyamani PS, Rondinelli JM. 2018. The must-have and nice-to-have experimental and computational requirements for functional frequency doubling deep-UV crystals. *Nat. Commun.* 9:2972
2. Mutailipu M, Pan S. 2020. Emergent deep-ultraviolet nonlinear optical candidates. *Angew. Chem. Int. Ed.* 59:20302–17
3. Ok KM. 2016. Toward the rational design of novel noncentrosymmetric materials: factors influencing the framework structures. *Acc. Chem. Res.* 49:2774–85
4. Halasyamani PS, Poeppelmeier KR. 1998. Noncentrosymmetric oxides. *Chem. Mater.* 10:2753–69
5. Tran TT, Yu H, Rondinelli JM, Poeppelmeier KR, Halasyamani PS. 2016. Deep ultraviolet nonlinear optical materials. *Chem. Mater.* 28:5238–58
6. Rondinelli JM, Kioupakis E. 2015. Predicting and designing optical properties of inorganic materials. *Annu. Rev. Mater. Res.* 45:491–518
7. Tokura Y, Kanazawa N. 2020. Magnetic skyrmion materials. *Chem. Rev.* 121:2857–97
8. Kanazawa N, Seki S, Tokura Y. 2017. Noncentrosymmetric magnets hosting magnetic skyrmions. *Adv. Mater.* 29:1603227
9. Wang J. 2019. Mechanical control of magnetic order: from phase transition to skyrmions. *Annu. Rev. Mater. Res.* 49:361–88
10. Felser C. 2013. Skyrmions. *Angew. Chem. Int. Ed.* 52:1631–34
11. Yang S-H, Naaman R, Paltiel Y, Parkin SSP. 2021. Chiral spintronics. *Nat. Rev. Phys.* 3:328–43
12. Göbel B, Mertig I, Tretiakov OA. 2021. Beyond skyrmions: review and perspectives of alternative magnetic quasiparticles. *Phys. Rep.* 895:1–28
13. Savage N. 2007. Ultraviolet lasers. *Nat. Photonics* 1:83–85
14. Yao W, He R, Wang X, Lin Z, Chen C. 2014. Analysis of deep-UV nonlinear optical borates: approaching the end. *Adv. Opt. Mater.* 2:411–17
15. Tressaud A, Poeppelmeier K. 2016. *Photonic and Electronic Properties of Fluoride Materials.* Prog. Fluor. Sci. Ser. Amsterdam: Elsevier
16. De Vivie-Riedle R, Troppmann U. 2007. Femtosecond lasers for quantum information technology. *Chem. Rev.* 107:5082–100
17. Zhang J-H, Clark DJ, Brant JA, Rosmus KA, Grima P, et al. 2020. α-Li$_2$ZnGeS$_4$: a wide-bandgap diamond-like semiconductor with excellent balance between laser-induced damage threshold and second harmonic generation response. *Chem. Mater.* 32:8947–55

18. Iyer AK, Cho JB, Waters MJ, Cho JS, Oxley BM, et al. 2022. Ba_2MAsQ_5 (Q = S and Se) family of polar structures with large second harmonic generation and phase matchability. *Chem. Mater.* 34:5283–93

19. Huang C, Zhang F, Pan S. 2023. Inorganic nonlinear optical materials. In *Comprehensive Inorganic Chemistry III*, ed. J Reedijk, KR Poeppelmeier, pp. 3–44. Amsterdam: Elsevier. **https://doi.org/10.1016/B978-0-12-823144-9.00081-9**

20. Kang L, Liang F, Jiang X, Lin Z, Chen C. 2020. First-principles design and simulations promote the development of nonlinear optical crystals. *Acc. Chem. Res.* 53:209–17

21. Halasyamani PS, Zhang W. 2017. Viewpoint: inorganic materials for UV and deep-UV nonlinear-optical applications. *Inorg. Chem.* 56:12077–85

22. Wu C, Yang G, Humphrey MG, Zhang C. 2018. Recent advances in ultraviolet and deep-ultraviolet second-order nonlinear optical crystals. *Coord. Chem. Rev.* 375:459–88

23. Wu H, Zhang B, Yu H, Hu Z, Wang J, et al. 2020. Designing silicates as deep-UV nonlinear optical (NLO) materials using edge-sharing tetrahedra. *Angew. Chem. Int. Ed.* 132:9007–11

24. Cheng H, Li F, Yang Z, Pan S. 2022. $Na_4B_8O_9F_{10}$: a deep-ultraviolet transparent nonlinear optical fluorooxoborate with unexpected short phase-matching wavelength induced by optimized chromatic dispersion. *Angew. Chem. Int. Ed.* 134:e202115669

25. Yu H, Zhang W, Young J, Rondinelli JM, Halasyamani PS. 2015. Design and synthesis of the beryllium-free deep-ultraviolet nonlinear optical material $Ba_3(ZnB_5O_{10})PO_4$. *Adv. Mater.* 27:7380–85

26. Hirschberger M, Nakajima T, Gao S, Peng L, Kikkawa A, et al. 2019. Skyrmion phase and competing magnetic orders on a breathing kagomé lattice. *Nat. Commun.* 10:5831

27. Hirschberger M, Nakajima T, Kriener M, Kurumaji T, Spitz L, et al. 2020. High-field depinned phase and planar Hall effect in the skyrmion host Gd_2PdSi_3. *Phys. Rev. B* 101:220401

28. Hirschberger M, Spitz L, Nomoto T, Kurumaji T, Gao S, et al. 2020. Topological Nernst effect of the two-dimensional skyrmion lattice. *Phys. Rev. Lett.* 125:076602

29. Khanh ND, Nakajima T, Yu X, Gao S, Shibata K, et al. 2020. Nanometric square skyrmion lattice in a centrosymmetric tetragonal magnet. *Nat. Nanotechnol.* 15:444–49

30. Kurumaji T, Nakajima T, Hirschberger M, Kikkawa A, Yamasaki Y, et al. 2019. Skyrmion lattice with a giant topological Hall effect in a frustrated triangular-lattice magnet. *Science* 365:914–18

31. Nomoto T, Koretsune T, Arita R. 2020. Formation mechanism of the helical Q structure in Gd-based skyrmion materials. *Phys. Rev. Lett.* 125:117204

32. Moreau-Luchaire C, Moutafis C, Reyren N, Sampaio J, Vaz CAF, et al. 2016. Additive interfacial chiral interaction in multilayers for stabilization of small individual skyrmions at room temperature. *Nat. Nanotechnol.* 11:444–48

33. Yasuda K, Wakatsuki R, Morimoto T, Yoshimi R, Tsukazaki A, et al. 2016. Geometric Hall effects in topological insulator heterostructures. *Nat. Phys.* 12:555–59

34. Matsuno J, Ogawa N, Yasuda K, Kagawa F, Koshibae W, et al. 2016. Interface-driven topological Hall effect in $SrRuO_3$-$SrIrO_3$ bilayer. *Sci. Adv.* 2:e1600304

35. Wang L, Feng Q, Kim Y, Kim R, Lee KH, et al. 2018. Ferroelectrically tunable magnetic skyrmions in ultrathin oxide heterostructures. *Nat. Mater.* 17:1087–94

36. Brown KR, Chiaverini J, Sage JM, Haffner H. 2021. Materials challenges for trapped-ion quantum computers. *Nat. Rev. Mater.* 6:892–905

37. Munn RW, Ironside CN, eds. 1993. *Principles and Applications of Nonlinear Optical Materials*. Dordrecht, Neth.: Springer

38. Kurtz SK, Perry TT. 1968. Powder technique for the evaluation of nonlinear optical materials. *J. Appl. Phys.* 39:3798–813

39. Ok KM, Chi EO, Halasyamani PS. 2006. Bulk characterization methods for non-centrosymmetric materials: second-harmonic generation, piezoelectricity, pyroelectricity, and ferroelectricity. *Chem. Soc. Rev.* 35:710–17

40. Nye JF. 1985. *Physical Properties of Crystals: Their Representation by Tensors and Matrices*. Oxford, UK: Clarendon

41. Maker PD, Terhune RW, Nisenoff M, Savage CM. 1962. Effects of dispersion and focusing on the production of optical harmonics. *Phys. Rev. Lett.* 8:21–22

42. Zhang W, Yu H, Wu H, Halasyamani PS. 2017. Phase-matching in nonlinear optical compounds: a materials perspective. *Chem. Mater.* 29:2655–68

43. Mutailipu M, Poeppelmeier KR, Pan S. 2020. Borates: a rich source for optical materials. *Chem. Rev.* 121:1130–202

44. Mutailipu M, Li F, Jin C, Yang Z, Poeppelmeier KR, Pan S. 2022. Strong nonlinearity induced by coaxial alignment of polar chain and dense [BO_3] units in $CaZn_2(BO_3)_2$. *Angew. Chem. Int. Ed.* 61:e202202096

45. Liu R, Wu H, Yu H, Hu Z, Wang J, Wu Y. 2021. $K_5Mg_2La_3(BO_3)_6$: an efficient, deep-ultraviolet nonlinear optical material. *Chem. Mater.* 33:4240–46

46. Ye N, Zeng W, Jiang J, Wu B, Chen C, et al. 2000. New nonlinear optical crystal $K_2Al_2B_2O_7$. *J. Opt. Soc. Am. B* 17:764–68

47. Ye N, Zeng W, Wu B, Chen C. 1998. Two new nonlinear optical crystals: $BaAl_2B_2O_7$ and $K_2Al_2B_2O_7$. In *Proceedings of the International Society for Optics and Photonics*, Vol. 3556, *Electro-Optic and Second Harmonic Generation Materials, Devices, and Applications II*, ed. C Chen. **https://doi.org/10.1117/12.318263**

48. Huang H, Liu L, Jin S, Yao W, Zhang Y, Chen C. 2013. Deep-ultraviolet nonlinear optical materials: $Na_2Be_4B_4O_{11}$ and $LiNa_5Be_{12}B_{12}O_{33}$. *J. Am. Chem. Soc.* 135:18319–22

49. Chen C, Wu B, Jiang A, You G. 1985. A new-type ultraviolet SHG crystal——β-BaB_2O_4. *Sci. China Ser. B* 28:235–43

50. Huang C, Mutailipu M, Zhang F, Griffith KJ, Hu C, et al. 2021. Expanding the chemistry of borates with functional [BO_2]$^-$ anions. *Nat. Commun.* 12:2597

51. Zhao S, Gong P, Bai L, Xu X, Zhang S, et al. 2014. Beryllium-free $Li_4Sr(BO_3)_2$ for deep-ultraviolet nonlinear optical applications. *Nat. Commun.* 5:4019

52. Tran TT, Koocher NZ, Rondinelli JM, Halasyamani PS. 2017. Beryllium-free β-$Rb_2Al_2B_2O_7$ as a possible deep-ultraviolet nonlinear optical material replacement for $KBe_2BO_3F_2$. *Angew. Chem. Int. Ed.* 56:2969–73

53. Li Y, Liang F, Zhao S, Li L, Wu Z, et al. 2019. Two non-π-conjugated deep-UV nonlinear optical sulfates. *J. Am. Chem. Soc.* 141:3833–37

54. Liu X, Gong P, Yang Y, Song G, Lin Z. 2019. Nitrate nonlinear optical crystals: a survey on structure-performance relationships. *Coord. Chem. Rev.* 400:213045

55. Mutailipu M, Yang Z, Pan S. 2021. Toward the enhancement of critical performance for deep-ultraviolet frequency-doubling crystals utilizing covalent tetrahedra. *Acc. Mater. Res.* 2:282–91

56. Shan P, Sun T, Chen H, Liu H, Chen S, et al. 2016. Crystal growth and optical characteristics of beryllium-free polyphosphate, $KLa(PO_3)_4$, a possible deep-ultraviolet nonlinear optical crystal. *Sci. Rep.* 6:25201

57. Wang S, Ye N. 2011. $Na_2CsBe_6B_5O_{15}$: An alkaline beryllium borate as a deep-UV nonlinear optical crystal. *J. Am. Chem. Soc.* 133:11458–61

58. Zhao S, Gong P, Luo S, Bai L, Lin Z, et al. 2014. Deep-ultraviolet transparent phosphates $RbBa_2(PO_3)_5$ and $Rb_2Ba_3(P_2O_7)_2$ show nonlinear optical activity from condensation of [PO_4]$^{3-}$ units. *J. Am. Chem. Soc.* 136:8560–63

59. Chen C, Wu Y, Li R. 1989. The anionic group theory of the nonlinear optical effect and its applications in the development of new high-quality NLO crystals in the borate series. *Int. Rev. Phys. Chem.* 8:65–91

60. Lei B-H, Pan S, Yang Z, Cao C, Singh DJ. 2020. Second harmonic generation susceptibilities from symmetry adapted Wannier functions. *Phys. Rev. Lett.* 125:187402

61. Tran TT, He J, Rondinelli JM, Halasyamani PS. 2015. $RbMgCO_3F$: a new beryllium-free deep-ultraviolet nonlinear optical material. *J. Am. Chem. Soc.* 137:10504–7

62. Tran TT, Young J, Rondinelli JM, Halasyamani PS. 2017. Mixed-metal carbonate fluorides as deep-ultraviolet nonlinear optical materials. *J. Am. Chem. Soc.* 139:1285–95

63. Tran TT, Halasyamani PS, Rondinelli JM. 2014. Role of acentric displacements on the crystal structure and second-harmonic generating properties of $RbPbCO_3F$ and $CsPbCO_3F$. *Inorg. Chem.* 53:6241–51

64. Ding Q, Liu X, Zhao S, Wang Y, Li Y, et al. 2020. Designing a deep-UV nonlinear optical fluorooxosilicophosphate. *J. Am. Chem. Soc.* 142:6472–76

65. Lei B-H, Yang Z, Yu H, Cao C, Li Z, et al. 2018. Module-guided design scheme for deep-ultraviolet nonlinear optical materials. *J. Am. Chem. Soc.* 140:10726–33

66. Li Y, Zhou Z, Zhao S, Liang F, Ding Q, et al. 2021. A deep-UV nonlinear optical borosulfate with incommensurate modulations. *Angew. Chem. Int. Ed.* 60:11457–63

67. Liang F, Kang L, Gong P, Lin Z, Wu Y. 2017. Rational design of deep-ultraviolet nonlinear optical materials in fluorooxoborates: toward optimal planar configuration. *Chem. Mater.* 29:7098–102

68. Liu X, Kang L, Gong P, Lin Z. 2021. LiZn(OH)CO$_3$: A deep-ultraviolet nonlinear optical hydroxycarbonate designed from a diamond-like structure. *Angew. Chem. Int. Ed.* 60:13574–78

69. Luo M, Song Y, Lin C, Ye N, Cheng W, Long X. 2016. Molecular engineering as an approach to design a new beryllium-free fluoride carbonate as a deep-ultraviolet nonlinear optical material. *Chem. Mater.* 28:2301–7

70. Mutailipu M, Zhang M, Yang Z, Pan S. 2019. Targeting the next generation of deep-ultraviolet nonlinear optical materials: expanding from borates to borate fluorides to fluorooxoborates. *Acc. Chem. Res.* 52:791–801

71. Peng G, Ye N, Lin Z, Kang L, Pan S, et al. 2018. NH$_4$Be$_2$BO$_3$F$_2$ and γ-Be$_2$BO$_3$F: overcoming the layering habit in KBe$_2$BO$_3$F$_2$ for the next-generation deep-ultraviolet nonlinear optical materials. *Angew. Chem. Int. Ed.* 57:8968–72

72. Shi G, Wang Y, Zhang F, Zhang B, Yang Z, et al. 2017. Finding the next deep-ultraviolet nonlinear optical material: NH$_4$B$_4$O$_6$F. *J. Am. Chem. Soc.* 139:10645–48

73. Wang Y, Zhang B, Yang Z, Pan S. 2018. Cation-tuned synthesis of fluorooxoborates: towards optimal deep-ultraviolet nonlinear optical materials. *Angew. Chem. Int. Ed.* 57:2150–54

74. Xiong L, Chen J, Lu J, Pan C-Y, Wu L-M. 2018. Monofluorophosphates: a new source of deep-ultraviolet nonlinear optical materials. *Chem. Mater.* 30:7823–30

75. Yu H, Zhang W, Young J, Rondinelli JM, Halasyamani PS. 2015. Design and synthesis of the beryllium-free deep-ultraviolet nonlinear optical material Ba$_3$(ZnB$_5$O$_{10}$)PO$_4$. *Adv. Mater.* 27:7380–85

76. Zhang B, Shi G, Yang Z, Zhang F, Pan S. 2017. Fluorooxoborates: beryllium-free deep-ultraviolet nonlinear optical materials without layered growth. *Angew. Chem. Int. Ed.* 56:3916–19

77. Peng G, Lin C, Fan H, Chen K, Li B, et al. 2021. Be$_2$(BO$_3$)(IO$_3$): The first anion-mixed Van der Waals member in the KBe$_2$BO$_3$F$_2$ family with a very strong second harmonic generation response. *Angew. Chem. Int. Ed.* 60:17415–18

78. Tran TT, Halasyamani PS. 2013. New fluoride carbonates: centrosymmetric KPb$_2$(CO$_3$)$_2$F and noncentrosymmetric K$_{2.70}$Pb$_{5.15}$(CO$_3$)$_5$F$_3$. *Inorg. Chem.* 52:2466–73

79. Luo M, Liang F, Song Y, Zhao D, Xu F, et al. 2018. M$_2$B$_{10}$O$_{14}$F$_6$ (M = Ca, Sr): two noncentrosymmetric alkaline earth fluorooxoborates as promising next-generation deep-ultraviolet nonlinear optical materials. *J. Am. Chem. Soc.* 140:3884–87

80. Harada JK, Charles N, Poeppelmeier KR, Rondinelli JM. 2019. Heteroanionic materials by design: progress toward targeted properties. *Adv. Mater.* 31:1805295

81. Kageyama H, Hayashi K, Maeda K, Attfield JP, Hiroi Z, et al. 2018. Expanding frontiers in materials chemistry and physics with multiple anions. *Nat. Commun.* 9:772

82. Tran TT, Gooch M, Lorenz B, Litvinchuk AP, Sorolla MG, et al. 2015. Nb$_2$O$_2$F$_3$: a reduced niobium (III/IV) oxyfluoride with a complex structural, magnetic, and electronic phase transition. *J. Am. Chem. Soc.* 137:636–39

83. Kunz M, Brown ID. 1995. Out-of-center distortions around octahedrally coordinated d^0 transition metals. *J. Solid State Chem.* 115:395–406

84. Goodenough JB, Longo JM. 1970. Crystallographic and magnetic properties of perovskite and perovskite-related compounds. In *Landolt-Börnstein: Group III Condensed Matter*, Vol. 4a, ed. KH Hellwege, AM Hellwege, pp. 126–314. Berlin: Springer-Verlag

85. Evans H. 1951. The crystal structure of tetragonal barium titanate. *Acta Crystallogr.* 4:377

86. Xue D, Zhang S. 1997. Comparison of non-linear optical susceptibilities of KNbO$_3$ and LiNbO$_3$. *J. Phys. Chem. Solids* 58:1399–402

87. Hou Y, Wu H, Yu H, Hu Z, Wang J, Wu Y. 2021. An effective strategy for designing nonlinear optical crystals by combining the structure-directing property of oxyfluorides with chemical substitution. *Angew. Chem. Int. Ed.* 133:25506–10

88. Abrahams SC, Reddy JM, Bernstein JL. 1966. Ferroelectric lithium niobate. 3. Single crystal X-ray diffraction study at 24°C. *J. Phys. Chem. Solids* 27:997–1012

89. Hewat A. 1973. Soft modes and the structure, spontaneous polarization and Curie constants of perovskite ferroelectrics: tetragonal potassium niobate. *J. Phys. C* 6:1074

90. Ok KM, Lee DW, Smith RI, Ohare D. 2012. Time-resolved in situ neutron diffraction under supercritical hydrothermal conditions: a study of the synthesis of $KTiOPO_4$. *J. Am. Chem. Soc.* 134:17889–91

91. Sykora RE, Ok KM, Halasyamani PS, Albrecht-Schmitt TE. 2002. Structural modulation of molybdenyl iodate architectures by alkali metal cations in $AMoO_3(IO_3)$ (A = K, Rb, Cs): a facile route to new polar materials with large SHG responses. *J. Am. Chem. Soc.* 124:1951–57

92. Halasyamani PS. 2004. Asymmetric cation coordination in oxide materials: influence of lone-pair cations on the intra-octahedral distortion in d^0 transition metals. *Chem. Mater.* 16:3586–92

93. Stoltzfus MW, Woodward PM, Seshadri R, Klepeis J-H, Bursten B. 2007. Structure and bonding in $SnWO_4$, $PbWO_4$, and $BiVO_4$: lone pairs versus inert pairs. *Inorg. Chem.* 46:3839–50

94. Walsh A, Payne DJ, Egdell RG, Watson GW. 2011. Stereochemistry of post-transition metal oxides: revision of the classical lone pair model. *Chem. Soc. Rev.* 40:4455–63

95. Nguyen SD, Yeon J, Kim S-H, Halasyamani PS. 2011. $BiO(IO_3)$: a new polar iodate that exhibits an aurivillius-type $(Bi_2O_2)^{2+}$ layer and a large SHG response. *J. Am. Chem. Soc.* 133:12422–25

96. Kim YH, Tran TT, Halasyamani PS, Ok KM. 2015. Macroscopic polarity control with alkali metal cation size and coordination environment in a series of tin iodates. *Inorg. Chem. Front.* 2:361–68

97. Chang H-Y, Kim S-H, Halasyamani PS, Ok KM. 2009. Alignment of lone pairs in a new polar material: synthesis, characterization, and functional properties of $Li_2Ti(IO_3)_6$. *J. Am. Chem. Soc.* 131:2426–27

98. Liu Y, Liu X, Liu S, Ding Q, Li Y, et al. 2020. An unprecedented antimony(III) borate with strong linear and nonlinear optical responses. *Angew. Chem. Int. Ed.* 59:7793–96

99. Roginskii EM, Kuznetsov VG, Smirnov MB, Noguera O, Duclere JR, et al. 2017. Comparative analysis of the electronic structure and nonlinear optical susceptibility of α-TeO_2 and β-TeO_3 crystals. *J. Phys. Chem. C* 121:12365–74

100. Xia M, Jiang X, Lin Z, Li R. 2016. "All-three-in-one": a new bismuth-tellurium-borate Bi_3TeBO_9 exhibiting strong second harmonic generation response. *J. Am. Chem. Soc.* 138:14190–93

101. Yang Y, Guo Y, Zhang B, Wang T, Chen Y-G, et al. 2022. Lead tellurite crystals $BaPbTe_2O_6$ and $PbVTe_5F$ with large nonlinear-/linear-optical responses due to active lone pairs and distorted octahedra. *Inorg. Chem.* 61:1538–45

102. Zhang W-L, Lin X-S, Zhang H, Wang J-Y, Lin C-S, et al. 2010. Lone electron-pair enhancement of SHG responses in eulytite-type compounds: $A^{II}_3M^{III}(PO_4)_3$ (A = Pb, M = Bi; A = Ba, M = Bi, La). *Dalton Trans.* 39:1546–51

103. Peng G, Yang Y, Tang Y-H, Luo M, Yan T, et al. 2017. Collaborative enhancement from Pb^{2+} and F^- in $Pb_2(NO_3)_2(H_2O)F_2$ generates the largest second harmonic generation effect among nitrates. *Chem. Commun.* 53:9398–401

104. Skyrme THR. 1961. A non-linear field theory. *Proc. R. Soc. A* 240:127–38

105. Skyrme THR. 1962. A unified field theory of mesons and baryons. *Nucl. Phys.* 31:556–69

106. Psaroudaki C, Panagopoulos C. 2021. Skyrmion qubits: a new class of quantum logic elements based on nanoscale magnetization. *Phys. Rev. Lett.* 127:067201

107. Dzyaloshinsky IE. 1958. A thermodynamic theory of "weak" ferromagnetism of antiferromagnetics. *Phys. Chem. Solids* 4:241–55

108. Moriya T. 1960. Anisotropic superexchange interaction and weak ferromagnetism. *Phys. Rev.* 120:91–98

109. Landau LD, Lifshitz EM. 1980. *Statistical Physics.* Oxford, UK: Butterworth-Heinemann

110. Kézsmárki I, Bordács S, Milde P, Neuber E, Eng LM, et al. 2015. Néel-type skyrmion lattice with confined orientation in the polar magnetic semiconductor GaV_4S_8. *Nat. Mater.* 14:1116–22

111. Wang Y, Rahman S, Sun E, Knill C, Zhang D, et al. 2021. From semiconducting to metallic: Jahn–Teller-induced phase transformation in skyrmion host GaV_4S_8. *J. Phys. Chem. C* 125:5771–80

112. Fujima Y, Abe N, Tokunaga Y, Arima T. 2017. Thermodynamically stable skyrmion lattice at low temperatures in a bulk crystal of lacunar spinel GaV_4Se_8. *Phys. Rev. B* 95:180410

113. Bordács S, Butykai A, Szigeti BG, White JS, Cubitt R, et al. 2017. Equilibrium skyrmion lattice ground state in a polar easy-plane magnet. *Sci. Rep.* 7:7584

114. Schueller EC, Kitchaev DA, Zuo JL, Bocarsly JD, Cooley JA, et al. 2020. Structural evolution and skyrmionic phase diagram of the lacunar spinel $GaMo_4Se_8$. *Phys. Rev. Mater.* 4:064402

115. Butykai Á, Geirhos K, Szaller D, Kiss LF, Balogh L, et al. 2022. Squeezing the periodicity of Néel-type magnetic modulations by enhanced Dzyaloshinskii-Moriya interaction of 4*d* electrons. *NPJ Quantum Mater.* 7:26

116. Routledge K, Vir P, Cook N, Murgatroyd PAE, Ahmed SJ, et al. 2021. Mode crystallography analysis through the structural phase transition and magnetic critical behavior of the lacunar spinel $GaMo_4Se_8$. *Chem. Mater.* 33:5718–29

117. Zuo JL, Kitchaev D, Schueller EC, Bocarsly JD, Seshadri R, et al. 2021. Magnetoentropic mapping and computational modeling of cycloids and skyrmions in the lacunar spinels GaV_4S_8 and GaV_4Se_8. *Phys. Rev. Mater.* 5:054410

118. Zhang H-M, Chen J, Barone P, Yamauchi K, Dong S, Picozzi S. 2019. Possible emergence of a skyrmion phase in ferroelectric $GaMo_4S_8$. *Phys. Rev. B* 99:214427

119. Kurumaji T, Nakajima T, Ukleev V, Feoktystov A, Arima T-H, et al. 2017. Néel-type skyrmion lattice in the tetragonal polar magnet $VOSe_2O_5$. *Phys. Rev. Lett.* 119:237201

120. Kurumaji T, Nakajima T, Feoktystov A, Babcock E, Salhi Z, et al. 2021. Direct observation of cycloidal spin modulation and field-induced transition in Néel-type skyrmion-hosting $VOSe_2O_5$. *J. Phys. Soc. Jpn.* 90:024705

121. Kim S-H, Halasyamani PS, Melot BC, Seshadri R, Green MA, et al. 2010. Experimental and computational investigation of the polar ferrimagnet $VOSe_2O_5$. *Chem. Mater.* 22:5074–83

122. Oyeka EE, Winiarski MJ, Blachowski A, Taddei KM, Scheie A, Tran TT. 2021. Potential skyrmion host $Fe(IO_3)_3$: connecting stereoactive lone-pair electron effects to the Dzyaloshinskii-Moriya interaction. *Chem. Mater.* 33:4661–71

123. Oyeka EE, Winiarski MJ, Sorolla M II, Taddei KM, Scheie A, Tran TT. 2021. Spin and orbital effects on asymmetric exchange interaction in polar magnets: $M(IO_3)_2$ (M = Cu and Mn). *Inorg. Chem.* 60:16544–57

124. Mathur N, Stolt MJ, Jin S. 2019. Magnetic skyrmions in nanostructures of non-centrosymmetric materials. *APL Mater.* 7:120703

125. Okuyama D, Bleuel M, White JS, Ye Q, Krzywon J, et al. 2019. Deformation of the moving magnetic skyrmion lattice in MnSi under electric current flow. *Commun. Phys.* 2:79

126. Yu XZ, Onose Y, Kanazawa N, Park JH, Han JH, et al. 2010. Real-space observation of a two-dimensional skyrmion crystal. *Nature* 465:901–4

127. Birch MT, Cortes-Ortuno D, Turnbull LA, Wilson MN, Gross F, et al. 2020. Real-space imaging of confined magnetic skyrmion tubes. *Nat. Commun.* 11:1726

128. Bocarsly JD, Heikes C, Brown CM, Wilson SD, Seshadri R. 2019. Deciphering structural and magnetic disorder in the chiral skyrmion host materials $Co_xZn_yMn_z$ (x+y+z = 20). *Phys. Rev. Mater.* 3:014402

129. Seki S, Yu XZ, Ishiwata S, Tokura Y. 2012. Observation of skyrmions in a multiferroic material. *Science* 336:198–201

130. Park HS, Yu X, Aizawa S, Tanigaki T, Akashi T, et al. 2014. Observation of the magnetic flux and three-dimensional structure of skyrmion lattices by electron holography. *Nat. Nanotechnol.* 9:337–42

131. Kautzsch L, Bocarsly JD, Felser C, Wilson SD, Seshadri R. 2020. Controlling Dzyaloshinskii-Moriya interactions in the skyrmion host candidates $FePd_{1-x}Pt_xMo_3N$. *Phys. Rev. Mater.* 4:024412

132. Karube K, Shibata K, White JS, Koretsune T, Yu XZ, et al. 2018. Controlling the helicity of magnetic skyrmions in a β-Mn-type high-temperature chiral magnet. *Phys. Rev. B* 98:155120

133. Yu XZ, Kanazawa N, Onose Y, Kimoto K, Zhang WZ, et al. 2011. Near room-temperature formation of a skyrmion crystal in thin-films of the helimagnet FeGe. *Nat. Mater.* 10:106–9

134. Tokunaga Y, Yu XZ, White JS, Rønnow HM, Morikawa D, et al. 2015. A new class of chiral materials hosting magnetic skyrmions beyond room temperature. *Nat. Commun.* 6:7638

135. Seki S, Garst M, Waizner J, Takagi R, Khanh ND, et al. 2020. Propagation dynamics of spin excitations along skyrmion strings. *Nat. Commun.* 11:256

136. Bocarsly JD, Need RF, Seshadri R, Wilson SD. 2018. Magnetoentropic signatures of skyrmionic phase behavior in FeGe. *Phys. Rev. B* 97:100404

137. Shanavas KV, Satpathy S. 2016. Electronic structure and the origin of the Dzyaloshinskii-Moriya interaction in MnSi. *Phys. Rev. B* 93:195101

138. Jena J, Stinshoff R, Saha R, Srivastava AK, Ma T, et al. 2019. Observation of magnetic antiskyrmions in the low magnetization ferrimagnet $Mn_2Rh_{0.95}Ir_{0.05}Sn$. *Nano Lett.* 20:59–65

139. Nayak AK, Kumar V, Ma T, Werner P, Pippel E, et al. 2017. Magnetic antiskyrmions above room temperature in tetragonal Heusler materials. *Nature* 548:561–66

140. Peng L, Takagi R, Koshibae W, Shibata K, Nakajima K, et al. 2020. Controlled transformation of skyrmions and antiskyrmions in a non-centrosymmetric magnet. *Nat. Nanotechnol.* 15:181–86

141. Meshcheriakova O, Chadov S, Nayak AK, Roessler UK, Kuebler J, et al. 2014. Large noncollinearity and spin reorientation in the novel Mn_2RhSn Heusler magnet. *Phys. Rev. Lett.* 113:087203

142. Bensaid D, Hellal T, Ameri M, Azzaz Y, Doumi B, et al. 2016. First-principle investigation of structural, electronic and magnetic properties in Mn_2RhZ (Z = Si, Ge, and Sn) Heusler alloys. *J. Supercond. Novel Magn.* 29:1843–50

143. Martinolich AJ, Neilson JR. 2017. Toward reaction-by-design: achieving kinetic control of solid state chemistry with metathesis. *Chem. Mater.* 29:479–89

144. Kovnir K. 2021. Predictive synthesis. *Chem. Mater.* 33:4835–41

145. Chamorro JR, McQueen TM, Tran TT. 2020. Chemistry of quantum spin liquids. *Chem. Rev.* 121:2898–934

146. Benavides KA, Oswald IWH, Chan JY. 2018. Casting a wider net: rational synthesis design of low-dimensional bulk materials. *Acc. Chem. Res.* 51:12–20

147. Latturner SE. 2018. Clusters, assemble: growth of intermetallic compounds from metal flux reactions. *Acc. Chem. Res.* 51:40–48

148. Maggard PA. 2021. Capturing metastable oxide semiconductors for applications in solar energy conversion. *Acc. Chem. Res.* 54:3160–71

149. Schmehr JL, Wilson SD. 2017. Active crystal growth techniques for quantum materials. *Annu. Rev. Mater. Res.* 47:153–74

150. Benedek NA, Hayward MA. 2022. Hybrid improper ferroelectricity: a theoretical, computational, and synthetic perspective. *Annu. Rev. Mater. Res.* 52:331–55

Contents

Indexes

Errata

An online log of corrections to *Annual Review of Materials Research* articles may be
found at http://www.annualreviews.org/errata/matsci